Journal of Power Sources 199 (2012) 75–84

Contents lists available at SciVerse ScienceDirect

Journal of Power Sources

journal homepage: www.elsevier.com/locate/jpowsour

Effects of catalyst load in Pt and Pb-based catalysts using formic acid oxidation as a model

G.S. Buzzo[a], M.J.B. Orlandi[a], E. Teixeira-Neto[b], P. Homem-de-Mello[a], A.C.G. Lopes[a], E. Franco-Junior[a], H.B. Suffredini[a,*]

[a] Universidade Federal do ABC, Centro de Ciências Naturais e Humanas, Rua Santa Adélia 166, Bairro Bangu, Santo André, SP, Brazil
[b] Universidade de São Paulo, Departamento de Química Fundamental, Av. Prof. Lineu Prestes, 748, Butantã, 05508-000 São Paulo, Brazil

ARTICLE INFO

Article history:
Received 5 September 2011
Received in revised form 11 October 2011
Accepted 12 October 2011
Available online 18 October 2011

Keywords:
Lead-based catalysts
Formic acid oxidation
HAADF-STEM
XEDS-SI
DFT

ABSTRACT

In this paper, we discuss the effects of catalyst load with respect to carbon powder for several Pt and Pb-based catalysts, using formic acid as a model molecule. The discussion is based on electrochemical tests, a complete morphological investigation and theoretical calculations. We show that the Pt and Pb-based catalysts presented activity in formic acid oxidation at very low catalyst loads (e.g., 0.5% in respect to the carbon content). Physical characterisations demonstrate that the electrodes are composed of separated phases of Pt and lead distributed in Pt nanometric-sized islands that are heterogeneously dispersed on the carbon support and Pb ultra-small particles homogeneously distributed throughout the entire carbon surface, as demonstrated by the microscopy studies. At high catalyst loads, very large clusters of Pb_xO_y could be observed. Electrochemical tests indicated an increase in the apparent resistance of the system (by a factor of 19.7 Ω) when the catalyst load was increased. The effect of lead in the materials was also studied by theoretical calculations (DFT). The main conclusion is that the presence of Pb atoms in the catalyst can improve the adsorption of formic acid in the catalytic system compared with a pure Pt-based catalyst.

1. Introduction

Several kinds of materials have been extensively studied for use as anodes in DLFCs (Direct Liquid Fuel Cells) [1–3]. This type of hardware has potential use in portable devices, especially those that operate using formic acid as fuel [4,5]. Among the metals, Pd can be considered a reference material [6,7]. However, other bi-metallic materials, including Pd–Pb alloys, have been shown as interesting choices to promote the oxidation of formic acid [8]. Casado-Rivera et al. [9] demonstrated that Pt–Pb and Pt–Bi catalysts were excellent candidates for use in DFAFC's (Direct Formic Acid Fuel Cells), exhibiting tolerance to CO poisoning, while Wang et al. [10] showed in an extensive work the effect of different bimetallic catalysts (Pt–Ru, Pt–Ir, Pt–Pb and Pt–Pd) on the oxidation of formic acid and methanol. Other publications by Alden et al. showed the enhancement of formic acid oxidation when the catalysts are synthesised by direct reduction of salts [11,12]. In addition, in a work published by Wang et al. [13], the authors suggested that the enhancement of ethanol oxidation in alkaline media was likely due to the so-called third-body effect, promoted by the presence of Pb in a Pd–Pt catalyst. Also, several kinds of synthesis routes are commonly used for the production of catalysts, resulting in different structures, such as core–shell structures [14], intermetallic [15] and non-intermetallic phases [16] and others. Among those methodologies, the sol–gel method appears to be a simple and effective technique for synthesising several types of catalysts [17].

One of the main aims in fuel cell research is focused on decreasing the use of noble metals to make cell technology economically viable, mainly due to the high cost of metals such as platinum and palladium [18]. Several studies have focused on the reduction of Pt in catalyst content [19]. Billy et al. [20] studied the impacts of ultra-low loadings of Pt in the cathode and anode. In this study, the authors demonstrated the possibility of using Pt loadings as low as 35 $\mu g\,Pt\,cm^{-2}$ in real fuel cell systems. In our work, a catalyst with a 0.5% catalyst load with respect to carbon black content was successfully tested.

The morphology of a 10% Pt–Pb/C material has already been described by our group using XRD information and a set of electron microscopy techniques, high resolution-transmission electron microscopy (HR-TEM), X-ray energy dispersive spectroscopy (XEDS-TEM) and chemical mapping by XEDS-spectrum imaging (XEDS-SI) [21]. The XED-spectroscopical investigation of this material unequivocally demonstrated the presence of Pb very small particles distributed on the carbon support, surrounding the Pt nanoparticles. In this previous work, the majority of the material was described as isolated Pt nanoparticles deposited on the carbon

* Corresponding author. Tel.: +55 11 4437 1600x434; fax: +55 11 4437 1600x804.
E-mail address: hugo.suffredini@ufabc.edu.br (H.B. Suffredini).

0378-7753/$ – see front matter © 2011 Elsevier B.V. All rights reserved.
doi:10.1016/j.jpowsour.2011.10.044

support surrounded by submicroscopic Pb oxide particles, which could not be imaged even by HR-TEM. In the present work, we use the high angle annular dark field technique in the scanning transmission electron microscope (HAADF-STEM) to reveal the spatial distribution of these PtO_x deposits and the Pt nanoparticles and compare the morphologies of the Pt–Pb/C materials prepared with increasing metal loads.

Because our catalysts are mainly constituted by lead oxides and lead atoms surrounding the heterogeneously dispersed Pt nanoparticle islands, as observed by the microscopy techniques, an initial theoretical approach was proposed in this work to attempt to understand the effect of the Pb atoms on catalysis. There are two main ways to study surfaces by quantum mechanics: the cluster and periodic slab approaches. The electrodes studied here are heterogeneous, and it is not simple to perform calculations with the usual theoretical methodologies, mainly because they are based on crystallographic distances between metallic atoms. Therefore, in this work, we have used a very simple model inspired by the Dipped Adcluster Model (DAM) to provide insight into the influence of different proportions of Pb and Pt on formic acid oxidation. This is a reasonable approach to obtain adsorption geometries and relative (but not absolute) adsorption energies, but it cannot obtain the real properties of the catalyst, such as band structure of the metal.

Thus, the present work aims to discuss the effect of catalyst load in Pt and Pb-based electrocatalysts for the oxidation of formic acid using electrochemical methods, microscopy studies and theoretical calculations as support. Despite its well-known toxicity, lead appears to be an interesting material for electrocatalysis.

2. Experimental

2.1. Working electrode preparation

A similar protocol has been described in previous publications [22,23], using an adapted sol–gel method as the synthesis route. Acetylacetonates of Pt and Pb were prepared in a mixture of ethanol and acetic acid (3:2, v/v) at appropriate concentrations and added to 0.2 g of carbon powder (Vulcan® XC72R) to achieve catalyst nominal loads of 0.5%, 1%, 10%, 20%, 30% and 40% (w/w, with respect to the carbon powder). The modified powders were treated for 1 h at a temperature of 400 °C under a nitrogen atmosphere.

Fixed quantities of 1000 μL water + 40 μL of a 5% Nafion® solution (5% in aliphatic alcohols) were added to a mixture containing 0.008 g of each modified powder. These mixtures were then transferred to an ultrasonic bath for 15 min to produce "black inks". Then, 5 μL of the ink was transferred to a glassy carbon electrode (geometric area of 0.031 cm^2) previously polished with alumina, and the samples were washed with isopropyl alcohol and dried in infrared light.

The total geometric area and quantity of ink deposited onto the glassy carbon electrode were maintained constant for all experiments, and the currents were not normalised in this paper, making it possible to use only the circulating currents in the process as the main magnitude to promote all comparative studies.

2.2. Reagents, apparatus and solutions

Similar protocols have been described in a previous publication [21]. Briefly, the electrochemical experiments were performed in a Pyrex® glass cell equipped with three electrodes. The reference electrode was a 3 mol L^{-1} KCl–Ag/AgCl system, and the auxiliary electrode was a 2 cm^2 Pt foil. The supporting electrolyte was a 0.5 mol L^{-1} H_2SO_4 solution (Merck), also containing 1.0 mol L^{-1} of formic acid (Synth). All electrochemical measurements were conducted in AUTOLAB PGSTAT 100 potentiostat/galvanostat equipment.

2.3. Morphological investigation and theoretical calculations

The crystalline structures of the investigated catalysts were determined using the powder X-ray diffraction (XRD) technique. Data were recorded with a Rigaku diffractometer (Miniflex model), using Cu Kα as the radiation source (1.5406 Å, 30 kV and 15 mA). Approximately 30 mg of the powdered samples was placed in a glass sample holder and compressed with a glass slide to obtain a uniform distribution. The 2θ Bragg angles were scanned over a range of 20–85° at a rate of 2° per minute with a 0.02° angular resolution. The size, shape, and spatial distributions of the catalyst crystallites deposited on the carbon were investigated by Transmission Electron Microscopy (TEM) with a JEOL JEM 2100 microscope operating at 200 kV. The catalyst was also investigated by acquiring Annular Dark-Field (HAADF) images with a high-resolution STEM FEI Titan 60–300 operating at 80 kV. The samples were prepared by ultrasonically treating the catalyst powders in isopropanol. A drop of the resulting dispersion was placed on thin carbon films, which were deposited on standard 400 mesh TEM copper grids and dried in air. The compositional distribution of the catalyst was investigated by either XEDS-TEM or XEDS-SI with a Digital Micrograph 1.8 system (Gatan Inc.) controlling a Thermo-Noran XEDS, performed by operating the instrument in the STEM mode. The SIs were acquired at a 20×20 pixel resolution with a dwell time of 2 s/pixel, using the drift correction facility every 100 s. XED-spectra were acquired in the 0–20 keV energy range at each pixel. Electron probe sizes of ca. 3 nm were obtained with the JEM 2100 instrument in STEM mode, allowing enough current density at each sample point for the acquisition of statistically significant X-ray counts for the investigated elements. The mean diameter distribution of the Pt–Pb crystallites was determined from the TEM images using the Image-Pro Plus 6.0 software. At least 400 nanoparticles were measured to build the presented particle size distribution histograms.

In this work, we used a very simple model inspired by the Dipped Adcluster Model (DAM) [24–26] to provide insight into the influence of Pb and Pt at different proportions on formic acid oxidation. This can be a reasonable approach for obtaining adsorption geometries and relative (but not absolute) adsorption energies, but it cannot be used to obtain properties such as band structure of the metal [27]. In this first theoretical approach, we decided to study initially the Pb influence on adsorption. In a next step, we intend to study also the influence of oxides.

All calculations were conducted by means of density functional theory (DFT), with the M06 functional and LanL2DZ basis set as implemented in the Gaussian 09 [28] program. M06 (and other functionals from Truhlar's group) is recommended to study thermochemistry, kinetics and noncovalent interactions and radical formation [29–31]. There are two common methods for studying surfaces by means of quantum mechanics: the cluster and the periodic slab approaches. Because the electrodes studied here are heterogeneous, it is hard to perform calculations with these usual theoretical methodologies, mainly because they are based on crystallographic distances between metallic atoms.

3. Results and discussion

3.1. Electrochemical studies

As commented in a previous publication [34], the determination of real areas for some materials using the hydrogen desorption technique is not effective because the hydrogen-UPD signal is commonly inhibited by the presence of the second metal. Also,

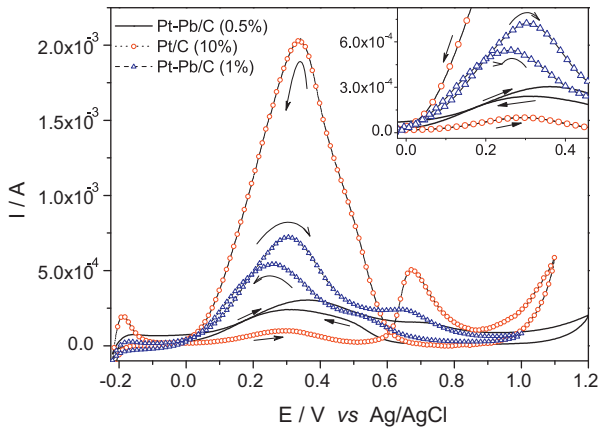

Fig. 1. Cyclic voltammetries for the Pt–Pb/C electrodes with nominal catalyst loads of 0.5% and 1% compared with a Pt/C catalyst with a nominal catalyst load of 10%. The inset represents a magnified view of onset oxidation regions. A scan rate of 20 mV s^{-1} was used for all tests.

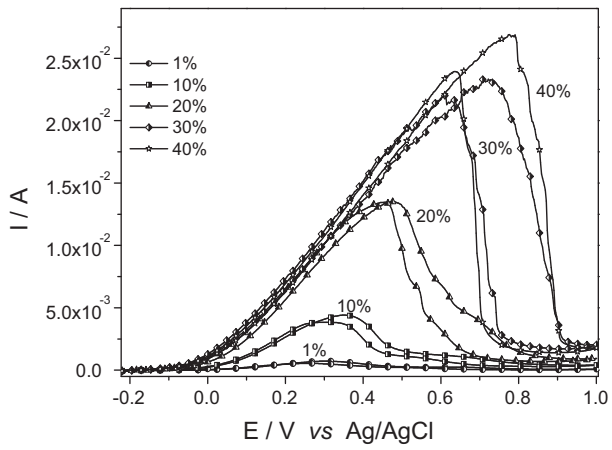

Fig. 2. Electrochemical responses to Pt–Pb/C catalysts with catalyst loads of 1%; 10%; 20%; 30%; 40% in the presence of 1.0 mol L^{-1} of formic acid (HCOOH) + 0.5 mol L^{-1} H_2SO_4 solution. A scan rate of 20 mV s^{-1} was used for all tests.

normalising the currents by CO desorption is not the best choice for several materials, including Pb-based catalysts, because these do not have affinity for carbon monoxide. Finally, normalising the currents by the total mass of catalyst (e.g., Pt) deposited onto the carbon powder is not interesting in this case because the main aim of this work was exactly to compare the differences between catalyst loads with respect to formic acid oxidation.

Thus, the currents were purposely presented as absolute currents (not normalised). Fig. 1 shows the initial electrochemical tests performed to compare the activity of catalysts Pt/C with 10% nominal load and Pt–Pb/C with 0.5% and 1% catalyst nominal load.

The cyclic voltammograms presented in Fig. 1 represent a comparison of the materials with 0.5% and 1.0% catalyst loads and a Pt/C catalyst with a 10% nominal load. Because Pt and Pb-based catalysts are composed of 50% of each metal, a 0.5% Pt and Pb-based catalyst contains 40-fold less platinum mass compared with a pure Pt-based electrode, as presented in Fig. 1. However, the oxidation response of the 0.5% catalyst is superior. This can be observed by the onset potential and currents of oxidation. The onset potential is less positive, and the currents of oxidation are visible higher than the Pb-containing material. This effect can best be observed in the inset of Fig. 1. The 1% catalyst load was plotted to facilitate the visualisation of the differences in electrochemical response. It is also possible to see that the Pt-based catalyst has an important affinity to the poisoning effect in this figure, presenting very high values of current in the return of the voltammetric cycle and becoming unviable for practical purposes. This effect (high currents in the return of the cycle) was not observed for the 0.5 and 1.0% catalyst load Pb-based electrodes.

Fig. 2 shows that increasing the catalyst load in the carbon powder substrate shifts the peak of oxidation to more positive potentials. Following the potentials, there is also an increase in the measured currents of oxidation. There are several processes, which may account for this kind of behaviour in a porous material, including mass transfer issues, electrical resistance, charge transfer resistance and formation of inhibiting oxides at the substrate. Several of them are non-ohmic in nature, but all of these factors contribute to the inhibition of electron flux. Thus, the discussion of resistance in this paper is better designed as an "apparent resistance", since that the origin of the resistance was not focused in this work.

Table 1 represents a collection of data extracted by the experiment shown in Fig. 2. The apparent resistance of the system was calculated as 19.7 Ω. The plot that appears to the right of

Table 1
Apparent resistance of the systems a function of catalyst load. The calculation was obtained from data extracted from Fig. 2. The graph to the right of the table represents the plot of the collected data to illustrate the resistivity effect.

Catalyst Load (%)	E / V (vs. Ag/AgCl)	I / A	
1	0.27	0.001	Apparent Resistance (Ω)
10	0.34	0.004	
20	0.44	0.013	19.7
30	0.71	0.023	
40	0.78	0.027	

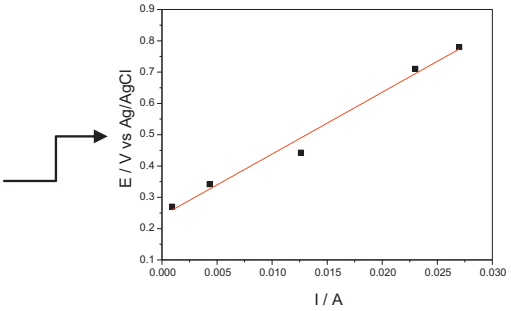

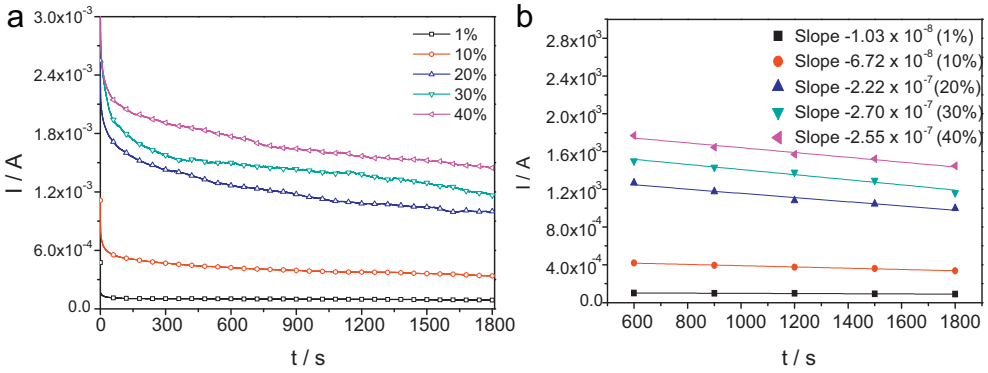

Fig. 3. Fast electrochemical response to Pt–Pb/C electrodes with catalyst loads of 1%; 10%; 20%; 30% and 40% in the presence of 1.0 mol L^{-1} formic acid (HCOOH) + 0.5 mol L^{-1} H_2SO_4 solution. (a) Short current–time responses at a fixed potential of 0.08 V vs. Ag/AgCl. (b) Linear fit at 5 different time points after stabilisation of the curve for all loads.

the table is only to illustrate the good correlation of the data. An increase in catalyst load has a visible influence on the apparent resistance of the system. This effect is probably related to the formation of Pb_xO_y. As an example, PbO_2 is a semiconductor material and a good candidate to promote this increase in the apparent resistance. Further studies are necessary to demonstrate this supposition.

Fast chronoamperometry studies (1800 s) are presented in Fig. 3(a) at a fixed potential of 0.08 V vs. Ag/AgCl. The currents of oxidation of formic acid also increase with catalyst load in this case, according to the voltammetric studies. Fig. 3(b) presents the slope at 5 different time points (600, 900, 1200, 1500 and 1800 s) for all studied catalysts. This figure illustrates that the higher the catalyst load, the higher the slope, as expected. This increase in slope is probably not associated with the consumption of HCOOH because the time of study was purposely very low. Despite the increase in the slope, the relative decrease in activity is practically constant for all studied catalyst (~19.0%) after 1200 s of operation (from 600 to 1800 s). As an example, the electrode with 40% of catalyst load presented an initial absolute current of 1.75×10^{-3} A. After 1200 s of operation, the absolute current was measured as being equal to 1.42×10^{-3} A. The total decrease in activity was calculated as 18.3%. Similar decrease of activity was observed for all studied catalysts.

Physical characterisation and morphological studies were conducted to understand the effect of catalyst load on the oxidation of formic acid. The next section presents an extensive study for selected catalysts.

3.2. Morphological investigation

3.2.1. X-ray diffraction

The diffraction patterns of the 10%, 20% and 40% Pt–Pb/C catalysts are presented in Fig. 4 to qualitatively identify the metal phases present within the crystalline domains of each material.

The broad reflection clearly observed at $2\theta = 25°$ in the 10% material is due to the (0 0 2) reflection from the carbon support. The relative intensity of this reflection decreases with the increase in catalyst metal loading (from 10% to 40%). The four main characteristic reflections from the face-centred cubic (fcc) structure of Pt within this 2θ range, namely from the planes (1 1 1), (2 0 0), (2 2 0) and (3 1 1), are seen in the XRD patterns of each material. The exact matching of these Pt reflections evidences the existence of separated crystallites of pure Pt in these Pt–Pb/C catalysts. The additional peaks observed for all materials match, but their relative intensities vary as a function of metal load. The correlation of these reflections with the ICDD Powder Diffraction Files (ICD-PDF) identifies the investigated materials as a mixture of different Pb oxides. Actually, the non-Pt particles within this material may be better described as a mixture of Pb_xO_y crystallites. The 10%, 20% and 40% catalysts are therefore formed by unalloyed, separated Pt and Pb_xO_y crystallites.

The size, shape and spatial distributions of the 10%, 20% and 40% Pt–Pb/C materials were analysed in detail by the acquisition of many images from different regions of the respective samples. A coherent description of the catalysts' morphologies can be made based on the bright-field TEM (BF-TEM) images presented in Fig. 5 and respective histograms of the particles' mean diameter distribution.

In the image of the 10% Pt–Pb/C material (Fig. 5), a grain of the carbon support is seen on a uniform gray background. The catalyst nanoparticles are the isolated small dark spots homogeneously distributed on the support. The particles have a general spheroidal shape, and the histogram shows a sharp size distribution with a mean diameter of 3.6 nm ± 2.4 nm. The 20% catalyst particles have a mean diameter of 6.2 nm ± 4.3 nm, and a broader size distribution was measured in the histogram. The particles appear irregularly distributed on the support, and some small particle aggregates are seen. In the 40% catalyst image, a large, dark gray particle is seen with smaller dark particles aggregated on it. The catalyst size distribution is even broader, and the majority of the particles (25%) have a size in the range of 30 nm to 270 nm. The mean diameter of the

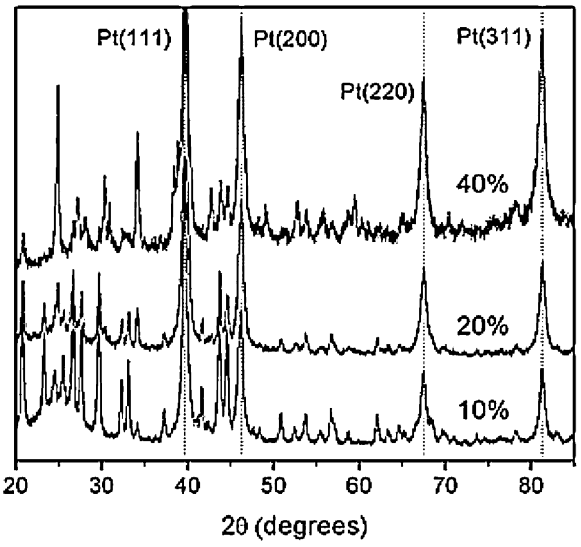

Fig. 4. X-ray diffraction patterns of Pt–Pb/C catalysts with metal loads of 10%, 20% and 40%. The exact matching of the indicated Pt reflections in all catalysts shows the existence of phase-separated Pt crystallites in the Pt–Pb/C materials.

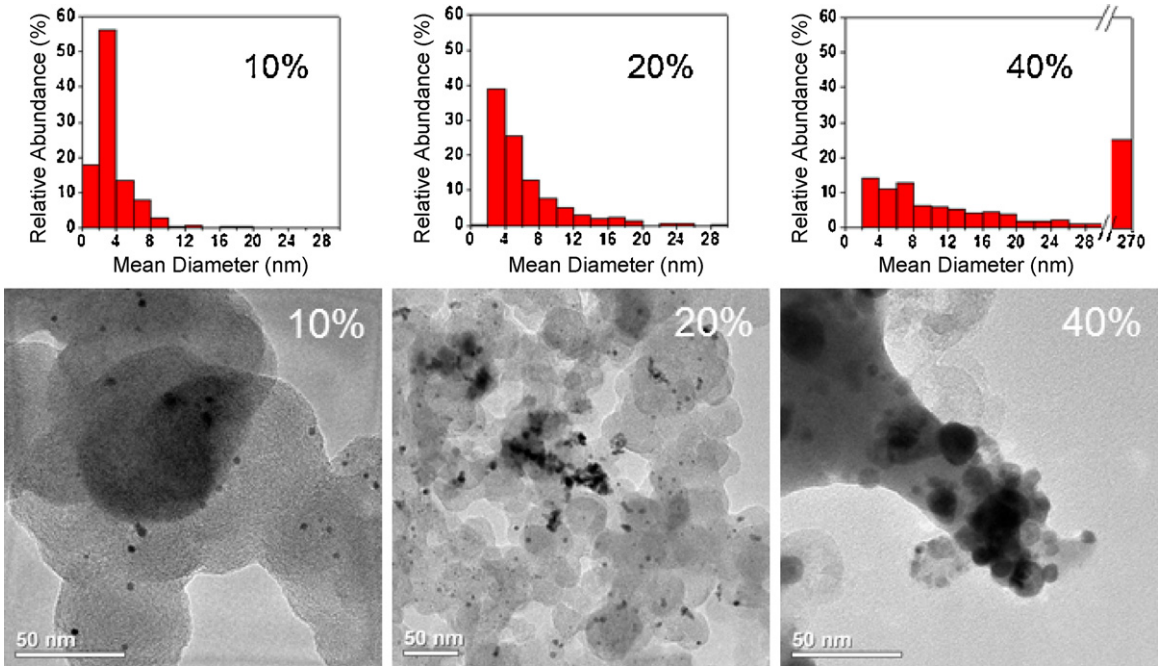

Fig. 5. BF-TEM images from representative regions of Pt–Pb/C catalysts with metal loads of 10%, 20% and 40% and their respective particles size distribution histograms. The morphological development from small and dispersed particles (10%) to aggregates of large particles (40%) is observed following the increase in catalyst metal load. Scale bars are 50 nm and have the same size for the 10% and 40% catalyst images. The 20% catalyst image was acquired at a lower magnification.

40% catalyst particles is 27.6 nm ± 40.9 nm. The observed increase in particle size and aggregation that follows the increase in catalyst metal load does not account for the spatial distribution of the metallic phases in these unalloyed materials.

The distribution of the metallic phases in the materials was investigated by the XEDS-SI chemical mapping of the catalysts. The BF-TEM image in Fig. 6 shows a representative region of the 10% Pt–Pb material. Non-aggregated particles, with sizes ranging from roughly 2 nm to 8 nm, are seen deposited on a bare carbon support. The area marked by a white square, which encloses one large particle, was divided into 20 × 20 pixels for the acquisition of an XEDS-SI.

The XED-spectrum in Fig. 6 was obtained from the SI data cube and shows the Pt Lα and Pb Lα counts measured in the marked area. A 150 eV energy window around the Pt Lα (9.44 keV) and Pb Lα (10.55 keV) peaks was used to construct the respective chemical maps. In the Pt map, brightness appears blurredly distributed at the position of the particle seen in the BF, while in the Pb map, brightness is distributed throughout the support. In a previous work, we hypothesized that the mapped Pb distribution arises from very small, highly dispersed Pb oxide deposits unobservable even by BF-HRTEM [21]. The presented chemical maps are blurred because of the use of an electron probe size (ca. 3 nm) larger than the selected pixel size (1.4 nm) and the sample drifting under the electron beam during SI acquisition. The use of such a large electron probe in the available LaB_6 electron gun instrument is a prerequisite for the generation of a suitable number of element X-ray counts at this high spatial resolution. The exact distribution of the Pb deposits on the support cannot be determined unless this material is investigated by a higher resolution technique. This was done by acquiring HAADF-STEM images, using an aberration-corrected field-emission gun instrument.

In the BF-TEM image of Fig. 7, a large particle with a size of roughly 16 nm is seen in the centre of the image with some smaller particles sized ca. 5 nm at the upper right quadrant of the image. Not any particle is seen deposited on the carbon support below the central large particle.

In the images acquired using the HAADF-STEM technique, the distribution of brightness is a function of the average atomic number of the sample (*z*-contrast images); brighter areas are from higher average atomic number areas of the sample. The HAADF-STEM image of Fig. 7 is from the same area imaged by BF-TEM. The central large particle seen in the BF image appears very bright at the top of the HAADF image, and many bright, irregularly shaped spots are seen on the carbon support. The existence of these high-average atomic number deposits dispersed on the carbon support may explain the distribution of Pb measured in the XEDS map of Fig. 6. The observed deposits are very small Pb particles dispersed throughout the support, surrounding the Pt nanoparticles.

The morphology of the 40% Pt–Pb/C catalyst was investigated by BF-STEM and XEDS-SI, which are shown in Fig. 8. In the BF image, the metal particles are the dark rounded areas deposited on a light gray carbon support. Two populations of different types of particles are seen: the two very large dark gray particles, at the centre and to the right of the image, and many smaller dark particles, dispersed on the dark gray particles and on the carbon support.

The catalyst metal distribution of the area marked with a square in the BF image was investigated by the acquisition of a XEDS-SI. The same electron probe size (ca. 3 nm) used for the acquisition of the SI in Fig. 6 was used to map the selected area (14 nm per pixel) to qualitatively determine the distribution of the metallic components of this catalyst. The darker particles in BF appear bright in the Pt map of Fig. 8, showing that they are composed of Pt, while the two larger dark gray particles in BF appear bright in the Pb map. The spatially resolved XED spectra (28 nm × 28 nm) from areas A and B, delimited by the squares in the elemental maps, are also in Fig. 8. Within area A, the dark particles deposited on the central large dark gray particle of the BF image cannot be seen, and not any Pt Lα X-ray count was accordingly measured within area A. Area B was drawn on a region with a dark particle aggregate in the BF image. Within this area, a considerable number of Pt Lα X-ray counts were measured. In both areas, approximately the same amount of Pb Lα X-ray counts were measured, showing that the small Pt particles are deposited on a large Pb oxide particle. The

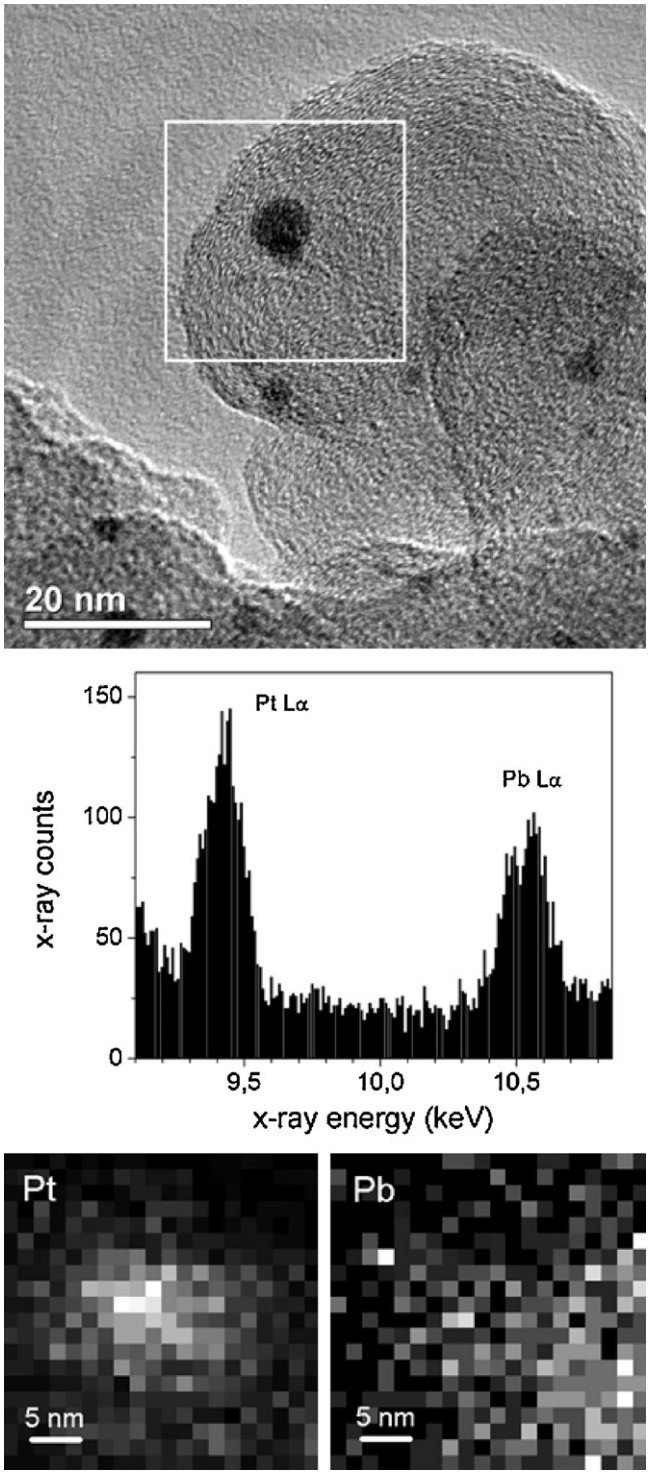

Fig. 6. BF-TEM image showing a region with non-aggregated 10% Pt–Pb/C catalyst particles and compositional XED-spectrum image information from the squared area. The Pt Lα and Pb Lα peaks measured within this area are in the XED-spectrum, and the respective chemical maps show that Pb is evenly distributed on the carbon support, while the measured Pt is directly associated with the position of the particle.

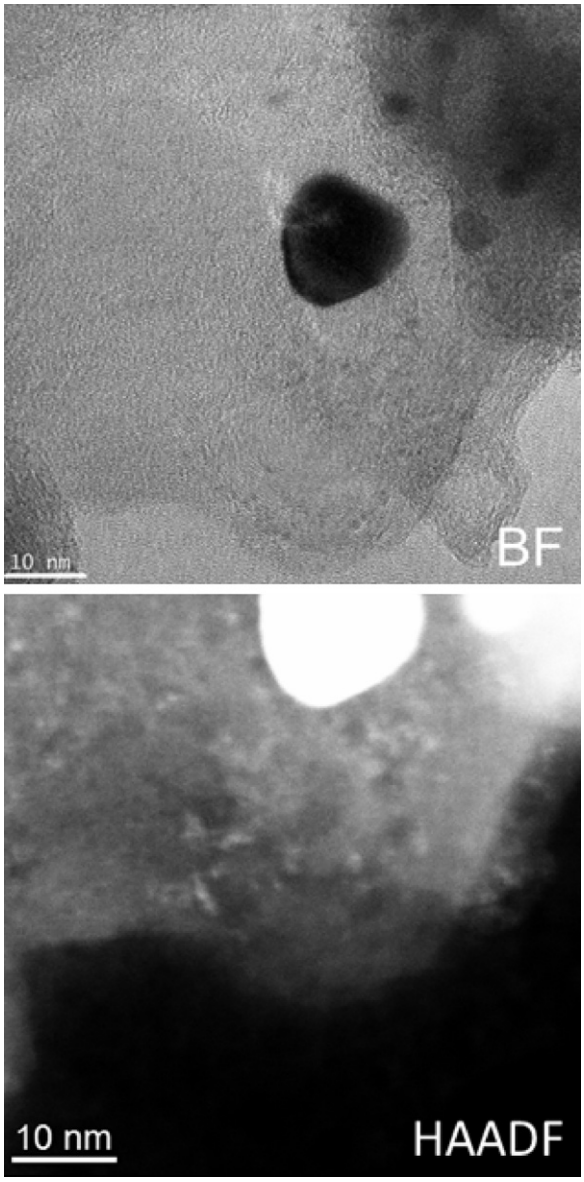

Fig. 7. BF-TEM and HAADF-STEM images from the same 10% Pt–Pb/C catalyst area. In the BF image, no particles are seen on the carbon support below the large central particle. In the HAADF image, small bright spots indicate the existence of very small, irregularly shaped metal particles deposited on the carbon support.

acquisition of many BF images and XEDS-SIs from different regions of the 40% Pt–Pb/C material shows that this catalyst is formed of large Pb_xO_y particles (parts of nanometres in size) surrounded by nanometre-sized Pt particles.

For this catalyst load, the increase in the apparent resistivities observed in the electrochemical studies can be associated with the formation of these large Pb_xO_y clusters, but further studies are necessary to demonstrate this supposition.

Conversely, the well dispersed Pb submicroscopic particles seem to have an important role in the catalysis. All the heterogeneously dispersed Pt islands are in contact with Pb atoms, homogeneously distributed on the entire carbon grain. Attempting to understand the role of lead in these catalysts, theoretical studies with a first approach were conducted. The results are presented in the next section.

3.3. Theoretical approach

As previously commented, a tentative explanation of the role of lead in the catalytic system is proposed. In this tentative, lead was simulated as being only in metallic form and lead oxide was not tested in this first approach. We have built electrodes consisting of four metallic atoms (with different proportions of Pt and Pb) as proposed by DAM, but as we do not know the distances between

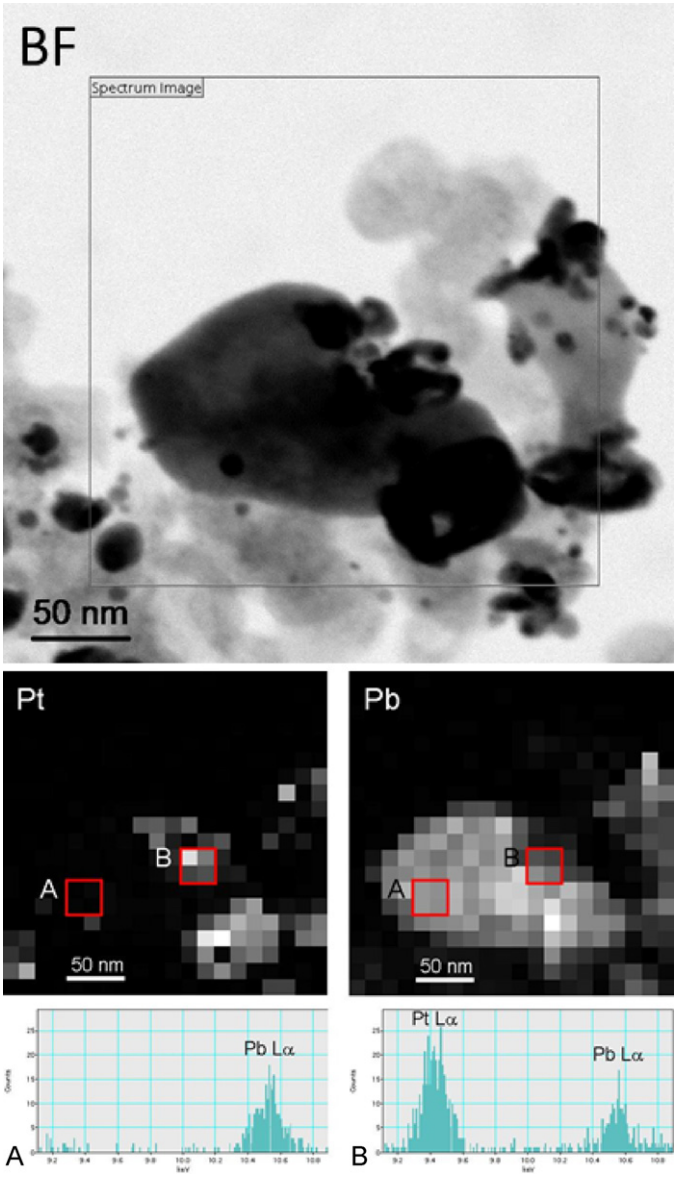

Fig. 8. BF-STEM image showing a region of the 40% Pt–Pb/C catalyst with two large particle aggregates, formed by dark particles deposited on larger dark gray particles, and Pt and Pb chemical maps from the squared area. The XED spectra A and B, measured from the A and B areas marked at both the Pt and Pb chemical maps, show that the large dark gray particles are Pb crystallites, while the smaller dark particles are Pt crystallites.

atoms, we fully optimised the geometries. Because in the experimental arrangement metallic atoms are supported on carbon, we inserted a saturated carbon chain under the metallic atoms, inducing them to stay together. Frequencies were calculated to ensure we obtained minima in the surface energy potential. Fig. 9 presents an electrode we used.

We studied the following compositions of the electrodes: pure Pt, 1Pb:3Pt and 2Pb:2Pt. Pb atoms were inserted at the extremity of the electrode and also alternated with Pt atoms.

The adsorbate, formic acid, was added to the electrodes (forming the "adcluster" system) always at the same distance but starting the optimisation process from different relative positions called A, B, C and D, as illustrated in Fig. 10. Formic acid intramolecular hydrogen bonding was avoided because we aimed to clearly differentiate between both oxygen atoms. We also fully optimised the system in this case, aiming to mimetise the preferred adsorption sites.

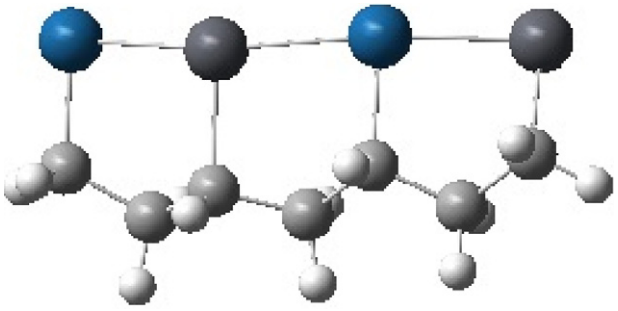

Fig. 9. The model used to represent electrodes. Bigger balls are metallic atoms (gray are lead atoms and blue platinum), light gray balls represent carbon atoms, and white balls are hydrogen atoms.

We calculated the adsorption energies for each adsorbate starting position for all electrode compositions. The oxidation process was simulated by extracting one and two electrons from the adcluster system.

Initially, we studied formic acid adsorption on Pt_4/C to compare the results obtained with DFT plane wave methodology [32,33]. Hartnig et al. [32] obtained several minimum energy configurations with the formic acid molecular plane perpendicular to the surface. When the C–H bond points towards the surface, it is elongated, even if in an uncharged surface. The authors calculated the adsorption energy as the difference between total energy of the adcluster and total energy of the isolated species. The lowest energy structure on the uncharged surface presented an adsorption energy of −0.37 eV and had both oxygen atoms pointed towards the surface. When C–H is pointed towards the surface, the adsorption energy is about −0.09 eV. In addition, Neurock and collaborators [33] have observed that formic acid oxidation occurs preferentially by a direct path to CO_2, in which there is an initial activation of the C–H bond that needs just one or two Pt atoms. In our calculations, even if our approach was very simplistic, it qualitatively reproduced those wave plane calculations for the Pt and formic acid interaction. For example, Fig. 11 presents two conformations and respective adsorption energies for the pure Pt electrode.

Table 2 presents the adsorption energies obtained for clusters formed by Pt and Pb atoms for all four formic acid starting points studied. When just one Pb atom is added to the Pt cluster, the adsorption energies are similar regardless of the position of the Pb atom in relation to the Pt atoms. If Pb is intercalated into Pt, the greatest (in modulus) adsorption energy corresponds to the D conformation. In contrast, if Pb is at the extremity of the cluster, conformations A and C have greater adsorption energies than that of intercalated Pb. Fig. 3 presents the structures obtained after the optimisation procedure for A and C conformations on the Pt–Pt–Pb–Pt cluster and A and D conformations on the Pt–Pt–Pt–Pb cluster. The first is the one with the smallest adsorption energy. In this case, formic acid is very distant from the Pb atom. In all other conformations, which correspond to greater adsorption energies, formic acid is nearer to the Pb atom. Particularly, the

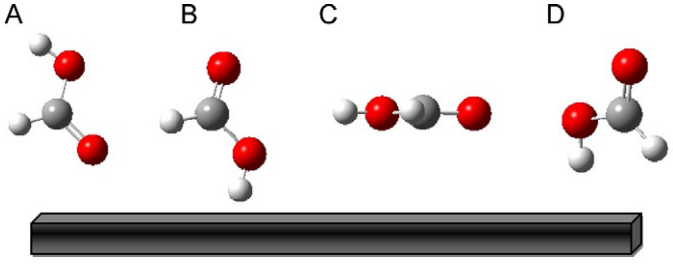

Fig. 10. Initial adsorbate positions A, B, C and D in relation to the model electrode.

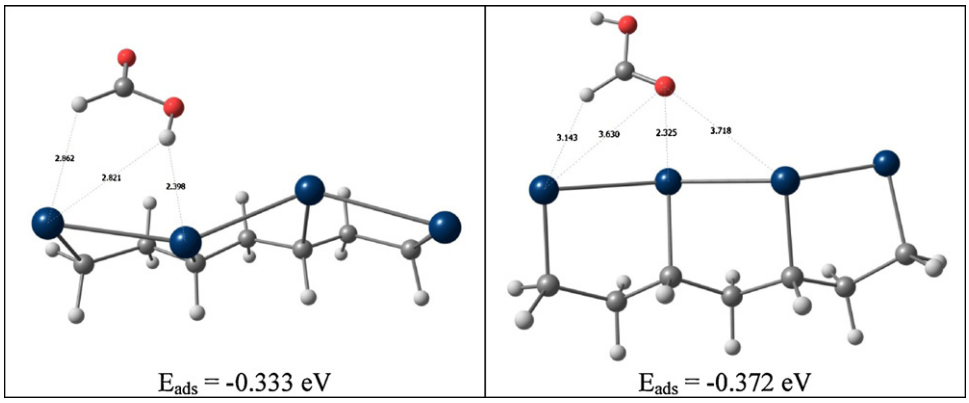

Fig. 11. Selected conformations of formic acid on a pure Pt cluster and their respective adsorption energies (E_{ads}, in eV).

C conformation of the Pt–Pt–Pt–Pb cluster has the C–H pointed towards a Pt atom (Figs. 12 and 13).

For the 2Pt:2Pb proportion, when Pt and Pb are intercalated, adsorption energies are similar to the 3Pt:1Pb proportion. However, when we have "dimers" of Pt and Pb side by side (Pt–Pt–Pb–Pb), adsorption energies are approximately four-fold greater. For A and C conformations on Pt–Pt–Pb–Pb, hydrogen is extracted from formic acid by Pt, and formate is adsorbed on Pb (Fig. 4).

Further calculations are necessary to fully understand the oxidation process. However, the adsorption energies and structures

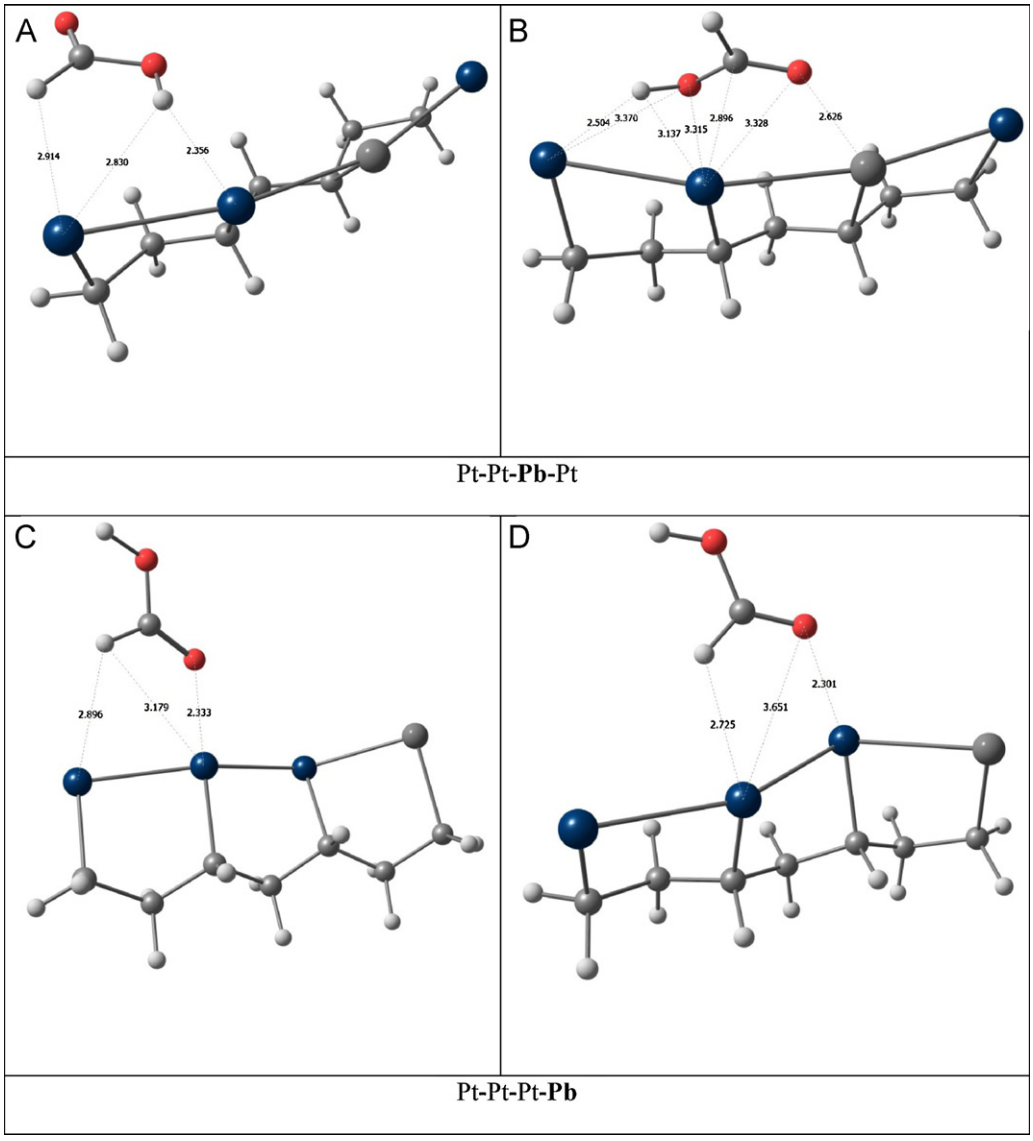

Fig. 12. Selected conformations on 3Pt:1Pb clusters.

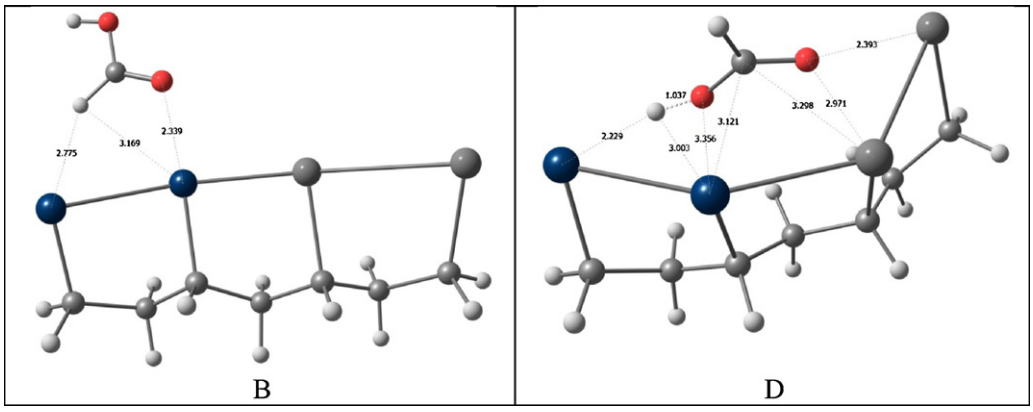

Fig. 13. Selected conformations on the Pt–Pt–Pb–Pb cluster.

Table 2
Adsorption energies (E_{ads}, in eV) obtained for the different conformations of formic acid on cluster compositions.

Cluster	Formic acid conformation	E_{ads} (eV)
Pt–Pt–Pb–Pt	A	−0.381075
	B	−0.410305
	C	−0.410301
	D	**−0.579966**
Pt–Pt–Pt–Pb	A	−0.446936
	B	−0.337830
	C	**−0.605246**
	D	−0.461282
Pt–Pb–Pt–Pb	A	**−0.472555**
	B	−0.392692
	C	0.008476
	D	−0.229678
Pt–Pt–Pb–Pb	A	−1.158709
	B	−0.393732
	C	−1.209029
	D	**−1.209041**

Bold represents the higher absolute energies for each conformation.

obtained by quantum chemistry calculations presented here provide insights about formic acid adsorption sites when electrodes are composed of Pt and Pb. Particularly, our calculations indicate that adsorption is favourable when there are "islands" of metals (as in the Pt–Pt–Pb–Pb cluster) instead of more homogeneous distributions (as in Pt–Pb–Pt–Pb cluster). These assumptions will be implemented in future wave plane calculations we intend to perform.

4. Conclusion

Physical characterisation demonstrated that the electrode was composed of separated phases of Pt and lead. The Pt and Pb-based catalysts presented activity in the formic acid oxidation at a very-low catalyst load (0.5% with respect to carbon content). These catalysts are composed mainly of Pt nanometric-sized islands heterogeneously dispersed onto the carbon support and Pb ultrasmall particles homogeneously distributed throughout the entire carbon surface, as demonstrated by the microscopy studies. The increase in the concentration of lead and platinum with respect to the carbon support promotes the formation of very large clusters of Pb_xO_y, which are not observed in catalysts with low catalyst loads, as shown in the TEM histograms. In addition, electrochemical tests indicate an increase in the apparent resistance of the system (to 19.7 Ω) when the catalyst load is increased. The catalytic effect probably occurs at the "Pt island/Pb submicroscopic particles" interface, since high-dispersed Pb atoms were observed throughout the entire carbon surface. At this Pb distribution, any island of Pt, homogeneously or heterogeneously dispersed, can find a Pb atom as a neighbour.

The effect of lead was also studied by a theoretical approach. Our preliminary studies showed that the presence of Pb atoms in the catalyst containing Pt can improve the adsorption of formic acid in the catalytic system if two atoms of lead appear neighbouring two atoms of Pt.

Acknowledgments

We thank the Brazilian agencies FAPESP (2007/05155-1, 2007/05370-0), CNPq (472476/2008-4, 301863/2008-3 and 483452/2010-6), CAPES, UFABC, LME-LNLS (JEOL JEM 2100 TEM-MSC) and DIMAT-INMETRO (FEI TITAN 80-300 STEM).

References

[1] N. Tian, Z.Y. Zhou, S.G. Sun, Y. Ding, Z.L. Wang, Science 316 (2007) 732–735.
[2] C.K. Rhee, B.J. Kim, C. Ham, Y.J. Kim, K. Song, K. Kwon, Langmuir 25 (2009) 7140–7147.
[3] U.B. Demirci, J. Power Sources 173 (2007) 11–18.
[4] C. Rice, S. Ha, R.I. Masel, A. Wieckowski, J. Power Sources 115 (2003) 229–235.
[5] C. Rice, S. Ha, R.I. Masel, P. Waszczuk, A. Wieckowski, J. Power Sources 111 (2002) 83–89.
[6] Y. Zhu, Z. Khan, R.I. Masel, J. Power Sources 139 (2005) 15–20.
[7] S. Ha, R. Larsen, Y. Zhu, R.I. Masel, Fuel Cells 4 (2004) 337–343.
[8] X.W. Yu, P.G. Pickup, J. Power Sources 192 (2009) 279–284.
[9] E. Casado-Rivera, D.J. Volpe, L. Alden, C. Lind, C. Downie, A.C.D. Angelo, F.J. DiSalvo, H.D. Abruña, J. Am. Chem. Soc. 126 (12) (2004) 4043–4049.
[10] J. Wang, P. Holt-Hindle, D. MacDonald, D.F. Thomas, A. Chen, Electrochim. Acta 53 (2008) 6944–6952.
[11] T. Ghosh, F. Matsumoto, J. McInnis, M. Weiss, H.D. Abruña, F.J. DiSalvo, J. Nanopart. Res. 11 (2009) 965–980.
[12] L.R. Alden, D.K. Han, F. Matsumoto, H.D. Abruña, F.J. DiSalvo, Chem. Mater. 18 (2006) 5591–5596.
[13] Y. Wang, T.S. Nguyen, X. Liu, X. Wang, J. Power Sources 195 (2010) 2619–2622.
[14] S. Patra, H. Yang, H. Bull, Korean Chem. Soc. 30 (2009) 1485–1488.
[15] C. Roychowdhury, F. Matsumoto, V.B. Zeldovich, S.C. Warren, P.F. Mutolo, M. Ballesteros, U. Wiesner, H.D. Abruña, F.J. DiSalvo, Chem. Mater. 18 (2006) 3365–3372.
[16] De-Jun Chen, Zhi-You Zhou, Q. Wang, Dong-Mei Xiang, N. Tian, Shi-Gang Sun, Chem. Commun. 46 (2010) 4252–4254.
[17] H.B. Suffredini, G.R. Salazar-Banda, L.A. Avaca, J. Power Sources 171 (2007) 355.
[18] H.A. Gasteiger, S.S. Kocha, B. Sompalli, F.T. Wagner, Appl. Catal. B: Environ. 56 (2005) 9–35.
[19] K. Sasaki, J.X. Wang, M. Balasubramanian, J. McBreena, F. Uribe, R.R. Adzic, Electrochim. Acta 49 (2004) 3873–3877.
[20] E. Billy, F. Maillard, A. Morin, L. Guetaz, F. Emieux, C. Thurier, P. Doppelt, S. Donet, S. Mailley, J. Power Sources 195 (2010) 2737–2746.
[21] E. Teixeira-Neto, G.S. Buzzo, H.B. Suffredini, J. Phys. Chem. C 114 (2010) 9227–9233.
[22] G.S. Buzzo, R.V. Niquirilo, H.B. Suffredini, J. Brazil. Chem. Soc. 21 (2010) 185–190.
[23] H.B. Suffredini, G.R. Salazar-Banda, L.A. Avaca, J. Sol–Gel Sci. Technol. 49 (2009) 131–136.
[24] J.L. Whitten, H. Yang, Surf. Sci. Rep. 24 (1996) 55–124.
[25] H. Nakatsuji, J. Chem. Phys. 87 (1987) 4995–5001.
[26] H. Nakatsuji, Progr. Surf. Sci. 54 (1997) 1–68.
[27] A.M. Pessoa, J.L.C. Fajin, J.R.B. Gomes, M.N.D.S. Cordeiro, J. Mol. Struct. Theochem. 946 (2010) 43–50.

[28] M.J. Frisch, Gaussian 03, Revision C.02, 2003.
[29] Y. Zhao, N.E. Schultz, D.G. Truhlar, J. Chem. Theory Comput. 2 (2006) 364–382.
[30] Y. Zhao, D.G. Truhlar, Acc. Chem. Res. 41 (2008) 157–167.
[31] Y. Zhao, D.G. Truhlar, J. Phys. Chem. A 112 (2008) 1095–1099.
[32] C. Hartnig, J. Grimminger, E. Spohr, J. Electroanal. Chem. 607 (2007) 133–139.
[33] M. Neurock, M. Janik, A. Wieckowski, Faraday Discuss. 140 (2009) 363–378.
[34] R.V. Niquirilo, E. Teixeira-Neto, G.S. Buzzo, H.B. Suffredini, Int. J. Electrochem. Sci. 5 (2010) 344–354.